

Solid-State Nuclear Magnetic Resonance Spectroscopic and Quantum Chemical Investigation of ^{13}C and ^{17}O Chemical Shift Tensors, ^{17}O Nuclear Quadrupole Coupling Tensors, and Bonding in Transition-Metal Carbonyl Complexes and Clusters

Renzo Salzmann,^{†,§} Martin Kaupp,^{*,‡} Michael T. McMahon,^{†,‡} and Eric Oldfield^{*,†}

Contribution from the Department of Chemistry, University of Illinois at Urbana-Champaign, 600 South Mathews Avenue, Urbana, Illinois 61801, and Max Planck Institut für Festkörperforschung, Stuttgart, Germany

Received September 9, 1997

Abstract: The carbon-13 and oxygen-17 nuclear magnetic resonance spectroscopic shielding behavior, as well as the oxygen-17 nuclear quadrupole coupling constants (NQCC), in the four metal–CO systems $\text{Fe}(\text{CO})_5$, $\text{Fe}_2(\text{CO})_9$, $\text{Ni}_2(\eta^5\text{-C}_5\text{H}_5)_2(\text{CO})_2$, and $\text{Rh}_6(\text{CO})_{16}$ have been investigated both experimentally and by density functional calculations. Characteristics of the spectroscopic observables and bonding for the most common types of metal–carbonyl coordination, μ_1 -, μ_2 -, and μ_3 -CO, may thus be compared in detail. There is generally very good agreement between the theoretical predictions and the experimental measurements, including the ^{17}O shift predictions for $\text{Fe}_2(\text{CO})_9$ and $\text{Rh}_6(\text{CO})_{16}$ made previously. Interestingly, the bridging oxygen shift tensor in $\text{Fe}_2(\text{CO})_9$ has its most deshielded component parallel to the C–O axis. This is highly unusual for carbonyl ligands, but is the normal behavior seen in organic carbonyl groups. To explain this and other observations, the computed shielding tensors and electric field gradients have been broken down into contributions from various localized, delocalized, or mixed sets of molecular orbitals. In addition to the common IGLO procedure, these analyses also include “partial IGLO” and IGLO-Pipek-Mezey methods. The results give new insights into both the magnitudes and orientations of the shielding and nuclear quadrupole coupling tensors. The potential for the combined use of solid-state NMR and quantum chemical methods in various areas of transition metal chemistry is discussed.

Introduction

Bonding between transition metals and carbonyl ligands is at the heart of many areas of chemistry. Examples range from organometallic synthesis to heterogeneous catalysis (e.g. surface-supported carbonyl complexes¹), as well as bioinorganic chemistry (e.g. carbonmonoxy–heme complexes²). NMR spectroscopy is one of the most important tools for the investigation of metal carbonyl complexes and clusters, and in the past, there have been several experimental studies of ^{13}C and ^{17}O chemical shifts in metal–CO systems in solution,^{3,4} as well as more limited studies in the solid state.^{5–10} In addition, for ^{17}O , the ^{17}O electric field gradient or quadrupole coupling constant has been measured in solution.¹¹ All of these parameters are expected to be sensitive to structure and bonding, which may vary considerably from one system to another.

In principle, the information contained in the observed NMR parameters (J -couplings, chemical shift tensors, nuclear quadrupole coupling tensors) exceeds by far that obtained from infrared and other spectroscopies. However, due to the complicated nature of these properties (they are tensors and depend

(3) (a) Lauterbur, P. C.; King, R. B. *J. Am. Chem. Soc.* **1965**, *87*, 3266–3267. (b) Aime, S.; Milone, L. *Prog. NMR Spectrosc.* **1977**, *11*, 183–211. (c) Aime, S.; Gobetto, R.; Osella, D.; Milone, L.; Hawkes, G. E.; Randall, E. W. *J. Magn. Reson.* **1985**, *65*, 308–315. (d) Aime, S.; Botta, M.; Gobetto, R.; Hanson, B. E. *Inorg. Chem.* **1989**, *28*, 1196–1198. (e) Hawkes, G. E.; Sales, K. D.; Aime, S.; Gobetto, R.; Lian, L.-Y. *Inorg. Chem.* **1991**, *30*, 1489–1493.

(4) (a) Hickey, J. P.; Wilkinson, J. R.; Todd, L. J. *J. Organomet. Chem.* **1979**, *179*, 159–168. (b) Aime, S.; Osella, D.; Milone, L.; Hawkes, G. E.; Randall, E. W. *J. Am. Chem. Soc.* **1981**, *103*, 5920–5922. (c) Aime, S. *Inorg. Chim. Acta* **1982**, *62*, 51–56.

(5) (a) Spiess, H.; Grosescu, R.; Haebleren, U. *Chem. Phys.* **1974**, *6*, 226–234. (b) Mahnke, H.; Sheline, R. K.; Spiess, H. W. *J. Chem. Phys.* **1974**, *61*, 55–60.

(6) (a) Dorn, H. C.; Hanson, B. E.; Mortell, E. *Inorg. Chim. Acta* **1981**, *L71*, 74. (b) Hanson, B. E.; Lisic, E. C.; Petty, J. T.; Iannaccone, G. I. *Inorg. Chem.* **1986**, *25*, 4062. (c) Aime, S.; Botta, M.; Gobetto, R.; Osella, D. *J. Chem. Soc., Dalton Trans* **1988**, 791–792.

(7) Walter, T. H.; Reven, L.; Oldfield, E. *J. Phys. Chem.* **1989**, *93*, 1320–1326.

(8) Gerathanassis, I. P.; Momenteau, M.; Barrie, P. J.; Kalodimos, C. G.; Hawkes, G. E. *Inorg. Chem.* **1996**, *35*, 2674–2679.

(9) Oldfield, E.; Keniry, M. A.; Shinoda, S.; Schramm, S.; Brown, T. L.; Gutowsky, H. S. *J. Chem. Soc., Chem. Commun.* **1985**, 791–793.

(10) Bodenbinder, M.; Balzer-Jöllenbeck, G.; Willner, H.; Batchelor, R. J.; Einstein, F. W. B.; Wang, C.; Aubke, F. *Inorg. Chem.* **1996**, *35*, 82–92.

(11) Aime, S.; Gobetto, R.; Osella, D.; Hawkes, G. E.; Randall, E. W. *J. Chem. Soc., Dalton Trans.* **1984**, 1863–1866.

[†] University of Illinois at Urbana-Champaign.

[§] Swiss National Science Foundation Postdoctoral Fellow, 1996–1997; American Heart Association, Illinois Affiliate, Postdoctoral Fellow, 1997–1998.

[‡] Max Planck Institut für Festkörperforschung.

[‡] National Institutes of Health Cellular and Molecular Biophysics Training Grant Trainee (Grant GM-08276).

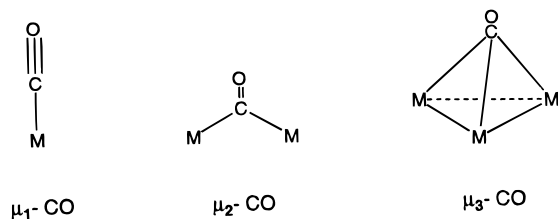
(1) See, e.g.: (a) Nagata, T.; Pohl, M.; Weiner, H.; Finke, R. G. *Inorg. Chem.* **1997**, *36*, 1366–1377. (b) Walter, T. H.; Thompson, A.; Keniry, M.; Shinoda, S.; Brown, T. L.; Gutowsky, H. S.; Oldfield, E. *J. Am. Chem. Soc.* **1988**, *110*, 1065–1068.

(2) See, e.g.: Antonini, E.; Brunori, M. *Hemoglobin and Myoglobin in their Reactions with Ligands*; North-Holland Publishing Co.: Amsterdam 1971. Perutz, M. F.; Fermi, G.; Luisi, G.; Shaanan, B.; Liddington, R. C. *Acc. Chem. Res.* **1987**, *20*, 309–321.

in a nontrivial way on various different factors¹²), their interpretation in terms of electronic structure is difficult. Here, quantum chemical methods can be of use in a number of ways. First, they should enable direct correlations between structure and spectra by permitting the prediction of spectra in systems having known structure. Second, they should enable qualitative bonding information to be obtained. And third, they should facilitate the refinement or prediction of the structures of materials in cases where there is uncertainty, such as in metalloproteins,⁸ by enabling the testing of different structural models, to see which structures permit the prediction of the spectroscopic observables.

During the past few years, density functional theory (DFT) has been shown to permit the accurate calculation of chemical shift tensors for ligands in transition metal complexes, by implicitly including the important effects of electron correlation at manageable computational cost.¹³ Indeed, there have already been initial studies of ¹³C and ¹⁷O nuclear shielding tensors for a range of carbonyl complexes and clusters.^{14–17} Most attention has been devoted to simple mononuclear complexes such as M(CO)₆ (M = Cr, Mo, W),^{14,15} which feature the typical large shift anisotropy expected for terminal carbonyl ligands. More unusual complexes of early transition metals in low oxidation states have also been studied theoretically and are predicted to exhibit a very low anisotropy for both carbon and oxygen shift tensors.¹⁶ Finally, it was shown for the clusters Fe₂(CO)₉ and Rh₆(CO)₁₆ that the small anisotropy of the ¹³C shift tensors for the bridging carbonyl ligands can be reproduced excellently by DFT calculations¹⁷—very low ¹⁷O shift anisotropies being predicted¹⁷ for the μ³-CO in the Rh₆(CO)₁₆ cluster.

In this paper, we expand upon these initial results and predictions by reporting a combined solid-state NMR and DFT study of the ¹³C and ¹⁷O shielding tensors for four systems: Fe(CO)₅, Fe₂(CO)₉, Ni₂(η⁵-C₅H₅)₂(CO)₂, and Rh₆(CO)₁₆. These complexes and clusters represent the most frequently encountered bonding arrangements (μ₁, μ₂, and μ₃) for carbonyl ligands:



In addition, we report the first measurements of their ¹⁷O nuclear quadrupole coupling constants (e^2qQ/h) in solid samples, again supplemented by DFT calculations. We find good accord between the experimental and theoretical results. A variety of procedures are used to interpret the computational results, based on a breakdown of contributions from various localized or delocalized molecular orbitals or combinations thereof, which allow us to go considerably beyond previous studies in relating the NMR spectroscopic observables to structure and bonding.

(12) See, e.g.: *Multinuclear NMR* Mason, J., Ed.; Plenum Press: New York, 1987.

(13) For a review see: *Computational NMR Studies of Transition Metal Compounds*; Kaupp, M.; Malkina, O. L.; Malkin, V. G. In *Encyclopedia of Computational Chemistry*; Schleyer, P. v. R., Ed.; Wiley-Interscience, New York, 1997/1998; in press.

(14) Kaupp, M.; Malkin, V. G.; Malkina, O. L.; Salahub, D. R. *Chem. Eur. J.* **1996**, *2*, 24–30.

(15) Ruiz-Morales, Y.; Schreckenbach, G.; Ziegler, T. *J. Phys. Chem.* **1996**, *100*, 3359–3367.

(16) Kaupp, M. *Chem. Eur. J.* **1996**, *2*, 348–358.

(17) Kaupp, M. *Chem. Ber.* **1996**, *129*, 527–533.

This should aid considerably in future studies on systems where less structural information is available such as in metalloproteins and their model systems.⁸

Experimental Section

Synthetic Aspects. Unless otherwise noted, all reactions and manipulations were performed in dry glassware with Schlenk techniques and standard freeze/pump/thaw techniques to degas solutions. Iron pentacarbonyl was freshly distilled prior to use, and all solvents were dried with standard methods. The other commercially available chemicals were used without further purification.

Fe(CO)₅ (1). The enrichment of Fe(CO)₅ with ¹³CO or ¹⁷O (Cambridge Isotope Laboratories, Cambridge, MA) was carried out by using a heterogeneous catalysis method.¹⁸ Fe(CO)₅ was exchanged with labeled CO for 30 min at room temperature, in the dark, using 5% Pd on Al₂O₃ as the catalyst for CO exchange. A small amount of benzene (~25% of the Fe(CO)₅ volume) was added prior to exchange. After exchange, 2 wt % Cr(acac)₃ was added to the filtrate. This acts as a T₁-relaxant for Fe(CO)₅, and is moderately soluble in benzene. Essentially quantitative (statistical) CO exchange was obtained, based on IR and mass spectrometry.

Fe₂(CO)₉ (2). The starting material, Fe(CO)₅, was enriched as described above, but using octane instead of benzene. Enriched Fe(CO)₅ solution (0.2 mL) was then transferred to a 20 mL Schlenk flask, 1 mL acetic acid was added, and the mixture was exposed under a slow nitrogen flow to a 200 W mercury vapor lamp for 1 h. The fine, golden, crystalline product was filtered off, washed once with cold ethanol and twice with ether, then dried under high vacuum for 15 min. The yield was 50%. Exposure over a longer period resulted in decomposition of the product, leading to a dark brown powder of high molecular weight, as evidenced by mass spectrometry.

Ni₂(η⁵-C₅H₅)₂(CO)₂ (3). The nickel dimer was synthesized by the method of King.¹⁹ A 150 mg sample of the dimer was then dissolved in 10 mL of degassed benzene and treated with 10 mg of Pd (10%) on Al₂O₃. Exposure to an enriched CO gas atmosphere over a period of 1 h, followed by filtration of the Pd/Al₂O₃ and removal of benzene, resulted in a dark green powder with nearly quantitative yield. The exchange, as measured by mass spectrometry, was quantitative.

Rh₆(CO)₁₆ (4). A solution of 85 mg of Rh₆(CO)₁₆ in 10 mL of degassed decalin was exposed to enriched CO gas, then heated at 140 °C for 40 h. The hot solution was then slowly cooled, and the Rh₆(CO)₁₆ crystals were filtered off and washed with cold cyclohexane, then ether. The product was dried in high vacuum for 15 min, again resulting in an almost quantitative yield. The exchange was 50% of the theoretical value, as measured via mass spectrometry.

NMR Spectroscopy. Solid-state NMR spectra were recorded with “home-built” spectrometers, which consist of 8.45 T 3.5 in. bore and 11.7 T 2.0 in. bore superconducting solenoid magnets (Oxford Instruments, Osney Mead, Oxford, UK), Tecmag (Houston, TX) Aries and Libra data systems, together with a variety of other digital and radio frequency circuitries. For radio frequency pulse amplification, we used Amplifier Research (Souderton, PA) and Henry Radio (Los Angeles, CA) transmitters. Solid-state spectra were obtained by using 5 mm Doty Scientific (Columbia, SC) “magic-angle” sample spinning (MAS) NMR probes. The 90° pulse widths for ¹³C varied from 3.5 to 5.0 μs, and for ¹⁷O the solid 90° pulse widths varied from 3 to 4.5 μs. Chemical shifts are reported with respect to tetramethylsilane (TMS) for ¹³C and water for ¹⁷O, both at 0 ppm, using the convention that high frequency, low-field, paramagnetic or deshielded values are positive (IUPAC δ-scale). For ¹³C, we used as a secondary standard the low-field peak of adamantane, taken to be 38.5 ppm downfield from TMS. For ¹⁷O, a tap water standard was used.

Shielding Tensor Determinations. We obtained the principal components of the ¹³C and ¹⁷O shielding tensor elements using the method of Herzfeld and Berger (HB),²⁰ modified to incorporate the

(18) (a) Webb, A. N.; Mitchell, J. J. *J. Phys. Chem.* **1959**, *63*, 1878–1885. (b) Noack, K.; Ruch, M. *J. Organomet. Chem.* **1969**, *17*, 302–322.

(19) King, R. B. *Organometallic Synthesis*; Academic Press: New York, 1965, Vol. 1, pp 119 and 120.

(20) Herzfeld, J.; Berger, A. *J. Phys. Chem.* **1980**, *73*, 6021–6030.

use of the Z-surface method.^{21,22} This approach uses Bayesian probability to deduce the μ, ρ terms of the HB equations. Typically, the shielding results of three spinning speeds were averaged, incorporating from 10 to 20 sidebands per spectrum, using a program kindly provided by Dr. H. Le.

Quantum Chemical Calculations of Nuclear Shieldings and Electric Field Gradients. Nuclear shieldings were calculated with the sum-over-states density-functional perturbation theory (SOS-DFPT) approach in its LOC1 approximation,^{23,24} using individual gauges for localized orbitals (IGLO).²⁵ All calculations of shieldings and of nuclear quadrupole couplings were carried out by using the gradient-corrected PW91 functional,²⁶ employing a version of the deMon program²⁷ (including the deMon-NMR modules^{23,24}) modified for the use of semilocal effective-core potentials (ECPs).

Quasirelativistic ECPs were used for the metals, with (8s7p6d)/[6s5p3d] Gaussian-type orbital valence basis sets.^{28,29} IGLO-II all electron basis sets²⁵ were used either for all ligand atoms (for Fe(CO)₅, Fe₂(CO)₉, and Ni₂(η^5 -C₅H₅)₂(CO)₂) or in a locally dense basis approximation for Rh₆(CO)₁₆, as described in ref 17. Further computational details are also as described previously¹⁷ for Fe₂(CO)₉ and Rh₆(CO)₁₆. For Fe(CO)₅, comparative calculations with the larger IGLO-III ligand basis sets²⁵ were also carried out. Experimental structures^{30–33} were used for all species. In the case of Ni₂(η^5 -C₅H₅)₂(CO)₂, the unreasonable experimental C–H distances were replaced by the more reasonable value of 1.094 Å. We implicitly take intermolecular contributions to shielding (and the electric field gradient) in these systems to be small, a view supported by, for example, the lack of any significant changes in isotropic shifts between solution and the solid state, as well as the observation that shift, shift tensor, and electric field gradient tensor results are well described theoretically by using the isolated complex structures.

Previous work has shown that, due to the complicated nature of the NMR chemical shift parameter, it is beneficial to employ different types of analyses in terms of molecular orbital (MO) contributions. Within an IGLO procedure, localized MO (LMO) contributions give useful insights. Alternatively, within a gauge-including atomic orbital (GIAO) framework,³⁴ or with a common gauge origin, a delocalized (canonical) MO analysis is feasible (with a common gauge, care has to be taken with respect to basis set convergence). Beyond these standard procedures, we have found two other variants to be useful. First, if within an IGLO-type treatment a few key orbitals (typically those

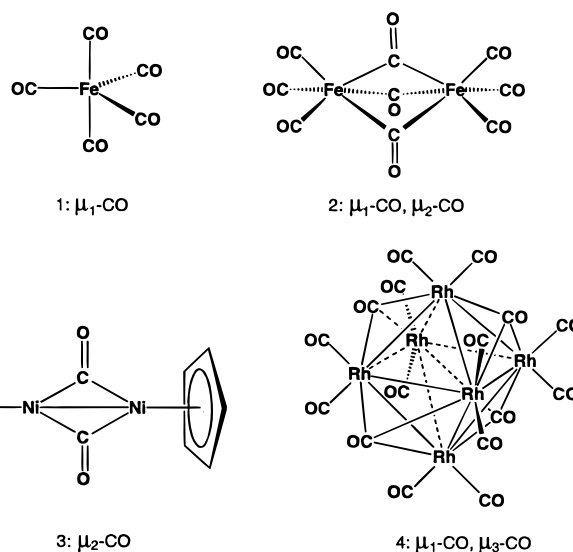
corresponding to delocalized cluster bonding) are excluded from the localization, a combined delocalized/localized analysis of the shielding tensor becomes possible. We will call this in the following a “partial IGLO”.³⁵ Second, in a recent DFT-IGLO study of ¹⁷O shieldings in transition-metal oxo complexes,³⁶ it was found that the usual IGLO method based on the Boys localization³⁷ was very sensitive to the way the semicore metal orbitals were localized (either separate from or together with the valence shell). In contrast, a modified IGLO procedure based on a Pipek-Mezey (PM) localization³⁸ (in the following denoted IGLO-PM) was more stable in this respect. As an additional feature, the PM localization provides σ – π separation in multiple bonds, even when no symmetry plane is present, whereas the Boys localization normally gives “banana bonds”. The σ – π separation is very useful for the analysis of shielding tensors in the present carbonyl ligands, as we describe below.

Computed absolute shieldings were converted to relative shifts via the theoretical absolute shieldings of TMS for ¹³C (187.5, 184.0 ppm with IGLO-II and IGLO-III bases, respectively) and H₂O_{liq} for ¹⁷O (271.0, 289.4 ppm, calculated from the computed absolute shieldings of H₂O_{vap} = 307.1, 325.5 ppm with IGLO-II and IGLO-III bases, and the experimental 36.1 ppm gas–liquid shift of water³⁹).

Nuclear quadrupole coupling constants were computed from the same Kohn–Sham orbitals employed for the nuclear shielding calculations, using the approach implemented in the deMon-NMR code.⁴⁰ The oxygen nuclear quadrupole moment was taken to be -0.02558 barn.⁴¹

Results and Discussion

We describe below our experimental and theoretical results on the following four compounds:



Fe(CO)₅, discussed as our first example, is of interest since it has both axial and equatorial CO ligands. Perhaps surprisingly, neither the ¹³C nor the ¹⁷O shielding tensor principal

(1) Le, H.; Pearson, J. G.; de Dios, A. C.; Oldfield, E. *J. Am. Chem. Soc.* **1995**, *117*, 3800–3807.

(2) Havlin, R. H.; McMahon, M.; Srinivasan, R.; Le, H.; Oldfield, E. *J. Phys. Chem.* **1997**, *101*, 8908–8913.

(3) Malkin, V. G.; Malkina, O. L.; Casida, M. E.; Salahub, D. R. *J. Am. Chem. Soc.* **1994**, *116*, 5898–5908.

(4) Malkin, V. G.; Malkina, O. L.; Eriksson, L. A.; Salahub, D. R. *Modern Density Functional Theory: A Tool for Chemistry: Theoretical and Computational Chemistry*; Seminario, J. M., Politzer, P., Eds.; Elsevier: Amsterdam, 1995; Vol. 2.

(5) Kutzelnigg, W.; Fleischer, U.; Schindler, M. *NMR—Basic Principles and Progress*; Springer: Heidelberg, 1990; Vol. 23, 165ff.

(6) (a) Perdew, J. P.; Wang, Y. *Phys. Rev. B* **1992**, *45*, 13244–13249. (b) Perdew, J. P. *Electronic Structure of Solids*; Ziesche, P., Eischrig, H., Eds.; Akademie Verlag: Berlin 1991. (c) Perdew, J. P.; Chevary, J. A.; Vosko, S. H.; Jackson, K. A.; Pederson, M. R.; Singh, D. J.; Fiolhais, C. *Phys. Rev. B* **1992**, *46*, 6671–6687.

(7) deMon program: Salahub, D. R.; Fournier, R.; Mlynarski, P.; Papai, I.; St-Amant, A.; Ushio, J. *Density Functional Methods in Chemistry*; Labanowski, J., Andzelm, J.; Springer: New York, 1991. St-Amant, A.; Salahub, D. R. *Chem. Phys. Lett.* **1990**, *169*, 387–392.

(8) Dolg, M.; Wedig, U.; Stoll, H.; Preuss, H. *J. Chem. Phys.* **1987**, *86*, 866–872.

(9) Andrae, D.; Häussermann, U.; Dolg, M.; Stoll, H.; Preuss, H. *Theor. Chim. Acta* **1990**, *77*, 123–141.

(10) Braga, D.; Grepioni, F.; Orpen, A. G. *Organometallics* **1993**, *12*, 1481–1483.

(11) Cotton, F. A.; Troup, J. M. *J. Chem. Soc., Dalton Trans.* **1974**, 800–802.

(12) Byers, L. R.; Dahl, L. F. *Inorg. Chem.* **1980**, *19*, 680–692.

(13) Corey, E. R.; Dahl, L. F.; Beck, W. *J. Am. Chem. Soc.* **1963**, *85*, 1202–1203.

(14) See, e.g.: (a) Ditchfield, R. *Mol. Phys.* **1974**, *27*, 789. (b) Wolinski, K.; Hinton, J. F.; Pulay, P. *J. Am. Chem. Soc.* **1990**, *112*, 8251–8260.

(35) As with calculations using a common gauge origin, care has to be taken with respect to basis set completeness. Moreover, this is not a black-box procedure, as symmetry and other requirements have to be considered (Kaupp, M.; Fleischer, U., to be published).

(36) Kaupp, M.; Malkina, O. L.; Malkin, V. G. *J. Chem. Phys.* **1997**, *106*, 9201–9212.

(37) Edmiston, C.; Ruedenberg, K. *Rev. Mod. Phys.* **1963**, *35*, 457–465. Edmiston, C.; Ruedenberg, K. *J. Chem. Phys.* **1965**, *43*, 597–602. Boys, S. F. *Quantum Theory of Atoms, Molecules and the Solid State*; Löwdin, P. O., Ed.; Academic Press: New York, 1966; pp 253ff. This procedure is often erroneously attributed to: Foster, J. M.; Boys, S. F. *Rev. Mod. Phys.* **1963**, *35*, 457–465.

(38) Pipek, J.; Mezey, P. G. *J. Chem. Phys.* **1989**, *90*, 4916–4926.

(39) See, e.g.: McFarlane, W.; McFarlane, H. C. E. in ref 12, pp 403ff.

(40) See, e.g.: Fedotov, M. A.; Malkina, O. L.; Malkin, V. G. *Chem. Phys. Lett.* **1996**, *258*, 330–335.

(41) Pyykkö, P. Z. *Naturforsch. A* **1989**, *47*, 189–196.

components have been reported previously, using MAS NMR methods (but they were predicted by DFT calculations¹⁵). For $\text{Fe}_2(\text{CO})_9$, there are in addition three μ_2 -CO groups. In this case, as well as is the case of $\text{Rh}_6(\text{CO})_{16}$ (containing μ_3 -CO groups), ^{17}O shielding tensor elements have also been predicted previously,¹⁷ but not determined experimentally. The third example, $\text{Ni}_2(\eta^5\text{-C}_5\text{H}_5)_2(\text{CO})_2$, is a more compact system containing (exclusively) μ_2 -CO groups, and was of interest primarily to investigate in which way the bridging CO shielding tensors depend on the nature of the metal atom. For the last system, $\text{Rh}_6(\text{CO})_{16}$, the focus will be on the μ_3 -CO ligands. In addition to the shift tensor determinations, our results with the ^{17}O -labeled systems have allowed us to make the first solid-state measurements of the ^{17}O electric field gradient (or the nuclear quadrupole coupling constant, NQCC), which can again be compared with the results of theoretical predictions, as discussed below.

(a) $\text{Fe}(\text{CO})_5$. The solution ^{13}C NMR spectrum of $\text{Fe}(\text{CO})_5$ was reported in 1958 by Cotton et al.,⁴² and ^{17}O shift results were published in 1962 by Bramley et al.⁴³ Solid-state ^{13}C results were then reported by Spiess et al.⁵ The conclusion of Spiess et al. was that there was fast exchange between the axial and the equatorial carbonyls, even at 4.2 K, but this conclusion was later questioned by Hanson.⁴⁴ Hanson, using MAS NMR, observed two different ^{13}C resonances at temperatures below -30 °C, having relative intensities of 2:3, consistent with the intensities expected for nonexchanging axial and equatorial carbonyls. However, a determination of the principal components of the tensors for each site was not reported. The first published tensor determinations for carbon-13 were derived from relaxation measurements in solution,⁵ although such determinations are quite difficult since they depend on an accurate determination of τ_c , the rotational correlation time. Indeed, these results differ considerably from the computational data of Ruiz-Morales et al.,¹⁵ using DFT-GIAO approaches. Solid-state NMR methods are the method of choice for experimentally determining the principal components of the ^{13}C and ^{17}O shielding tensors, but such studies are not particularly attractive, due to the extreme volatility and toxicity of $\text{Fe}(\text{CO})_5$.

We therefore devised a protocol that enables the low-T MAS NMR of $\text{Fe}(\text{CO})_5$. There are two major problems. The first is that it is a nontrivial matter to spin $\text{Fe}(\text{CO})_5$ at low temperatures. Most conventional rotors are prone to leak, or seals may crack at low T. The second problem is that the spin–lattice relaxation times of $\text{Fe}(\text{CO})_5$ become very long at low T, since there are no effective relaxation mechanisms. For example, T_1 has been reported to be ~ 30 min at -60 °C.⁴⁵

One solution to these problems is to use sealed ampules (to prevent leakage), to which small amounts of benzene (to enable cross-polarization) and $\text{Cr}(\text{acac})_3$ (to reduce T_1) are added. Our protocol is thus as follows: $^{13}\text{C}/^{17}\text{O}$ -enriched $\text{Fe}(\text{CO})_5$, diluted with benzene and a small amount of $\text{Cr}(\text{acac})_3$, was transferred via syringe to a glass insert (obtained from Wilmad Glass Company, Buena, NJ). The insert was then sealed in the dark, using a drop of fast-curing epoxy that had been shown to be resistant to iron pentacarbonyl (GC Electronics, 5 min epoxy; Rockford, IL) as shown schematically in Figure 1. After this layer dried in the dark for 30 min, a slow-curing epoxy layer was applied on top of the first layer, Figure 1, and allowed to

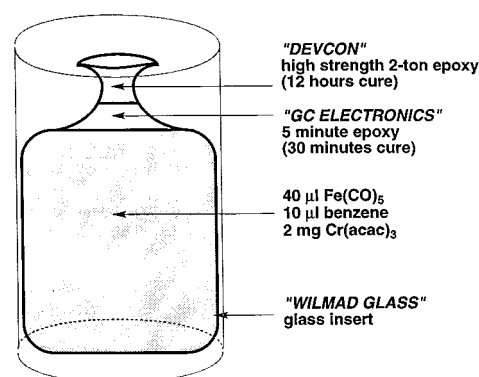


Figure 1. Schematic of the sealed sample cell used for ^{13}C , ^{17}O MAS NMR investigations of $\text{Fe}(\text{CO})_5$ at low temperatures.

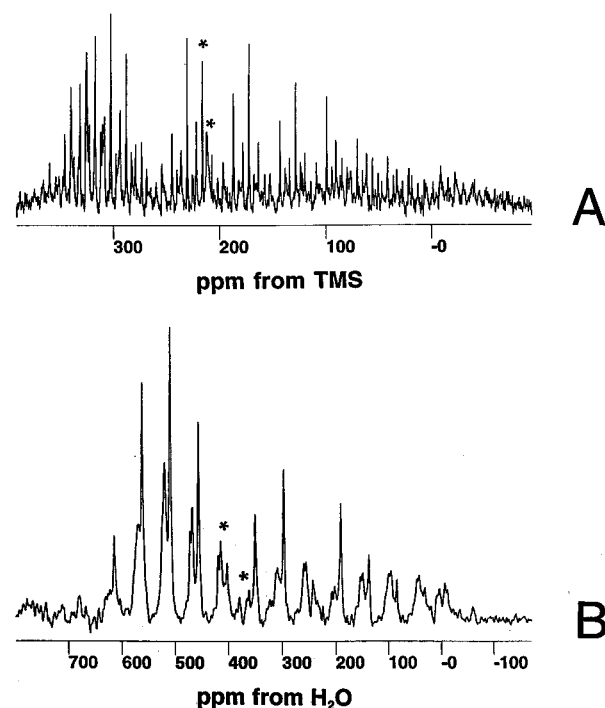


Figure 2. Solid-state NMR spectra of $\text{Fe}(\text{CO})_5$ (plus C_6H_6 and $\text{Cr}(\text{acac})_3$) at -120 °C: (A) 125.6 MHz ^{13}C cross-polarization magic-angle sample spinning spectrum, 3 ms mix time, spinning speed = 1820 ± 5 Hz; (B) 67.8 MHz ^{17}O proton-decoupled spectrum, 3600 ± 5 Hz spinning speed, 20 Hz line broadening due to exponential multiplication. The recycle times were 5 s in both cases. The centerbands are indicated with an asterisk.

cure in the dark for 12 h. This second epoxy layer was stable down to -150 °C, without cracking. All manipulations were carried out in an inert atmosphere (glovebag). With this arrangement, data acquisition was possible using recycle times as short as 5 s, enabling relatively high signal-to-noise ratio spectra for both ^{13}C and ^{17}O , Figure 2.

We then used the Herzfeld–Berger method to deduce the principal components of the ^{13}C and ^{17}O shielding tensors, for both the axial and equatorial sites. The results obtained are shown in Table 1. These experimentally determined shifts and shift tensors are both in good accord with those predicted theoretically, as shown in Table 1. The carbon shifts predicted previously at the DFT-GIAO level by Ruiz-Morales et al.¹⁵ are somewhat larger than the experimental values as well as our computations. This may partially be due to the fact that the DFT-GIAO calculations employed the uncoupled DFT approach (neglecting the SOS-DFPT correction terms^{23,24} included here, which reduce the paramagnetic contributions to some extent).

(42) Cotton, F. A.; Danti, A.; Waugh, J. S.; Fessenden, R. W. *J. Chem. Phys.* **1958**, *29*, 1427.

(43) Bramley, R.; Figgis, B. N.; Nyholm, R. S. *Trans. Faraday Soc.* **1962**, *58*, 1893–1896.

(44) Hanson, B. E. *J. Am. Chem. Soc.* **1989**, *111*, 6442–6443.

(45) Hanson, B. E.; Whitmire, K. E. *J. Am. Chem. Soc.* **1990**, *112*, 974–977.

Table 1. Comparison of Experimental and Computed Isotropic Shifts, Shift Tensor Elements, and Shift Anisotropies

system	site		shifts and shift anisotropy values (ppm)					$\delta_{33} - \delta_{11}$	$\delta_{22} - \delta_{11}$
			δ_{iso}	δ_{11}	δ_{22}	δ_{33}			
Fe(CO) ₅	C _{axial}	exptl ^a	215	345	345	−30	375	0	
		calcd (II)	210	334	334	−39	373	0	
		calcd (III)	219	347	347	−38	385	0	
		calcd ^b	236	366	366	−24	390	0	
	C _{equatorial}	exptl ^a	207	354	341	−60	414	13	
		calcd (II)	206	341	333	−58	399	8	
		calcd (III)	213	353	346	−59	412	7	
		calcd ^b	221	363	359	−58	421	4	
	O _{axial}	exptl	401	588	588	28	560	0	
		calcd (II)	349	524	524	5	519	0	
		calcd (III)	383	556	556	34	522	0	
		calcd ^b	391	574	574	26	548	0	
	O _{equatorial}	exptl	362	627	545	−25	652	82	
		calcd(II)	334	567	495	−60	627	72	
calcd(III)		369	604	534	−30	634	70		
calcd ^b		356	609	531	−70	679	78		
Fe ₂ (CO) ₉	C _{terminal}	exptl	205	346	346	−65	411	0	
		calcd ^c	213	350	346	−58	408	4	
	C _{bridge}	exptl	239	300	260	153	147	40	
		calcd ^c	257	314	260	196	118	54	
	O _{terminal}	exptl	380	617	592	−69	686	25	
		calcd ^c	359	579	569	−70	649	10	
	O _{bridge}	exptl	630	763	696	431	332	67	
		calcd ^c	586	728	659	370	358	69	
Ni ₂ (η^5 -C ₅ H ₅) ₂ (CO) ₂	C _{bridge}	exptl	226	326	247	106	220	79	
		calcd	233	296	289	114	182	7	
	O _{bridge}	exptl	504	604	500	407	197	93	
		calcd	472	563	499	351	212	64	
Rh ₆ (CO) ₁₆	C _{terminal}	exptl ^d	180	315	305	−80	395	10	
		exptl ^e	181	320	299	−76	396	21	
		calcd ^c	189	335	311	−80	415	24	
	C _{bridge}	exptl ^d	231	296	296	102	194	0	
		exptl ^e	230	301	292	97	204	9	
		calcd ^c	231	293	293	106	187	0	
	O _{terminal}	exptl	364	617	509	−34	651	108	
		calcd ^c	326	554	485	−62	616	69	
	O _{bridge}	exptl	563	616	568	505	111	48	
		calcd ^c	572	589	589	537	52	0	

^a Previously obtained isotropic carbon shifts of 216 ppm (C_{ax}) and 208 ppm (cf. ref 44) agree well with our results. ^b Absolute shieldings from ref 15 have been converted to relative shift by using the shieldings computed here for TMS and H₂O (see Computational Details section). ^c Cf. ref 17. ^d Cf. ref 49. ^e Cf. ref 7.

Note, however, that expansion of the ligand basis from IGLO-II to IGLO-III also increases our computed shifts slightly. Moreover, Ruiz-Morales et al. had reported only absolute shieldings, and no shieldings for TMS or H₂O, respectively. Thus, we used our own shielding values for the reference molecules (cf. computational details section). This may also give a slight bias to the computed shifts.

Figures 3 and 4 illustrate the generally very good accord between the present theoretical and experimental shift tensor determinations for all four compounds investigated (for consistency, the IGLO-II results were used for Fe(CO)₅). We find for the isotropic ¹³C shifts a slope of 0.98 and an *R*² value of 0.92 (Figure 3A), while for ¹⁷O the results are a slope of 0.89 and an *R*² value of 0.94 (Figure 4A), to be compared with ideal values of 1, 1. For the tensor elements, we obtain for ¹³C a slope of 0.99 and *R*² = 1.00 (Figure 3B) and for ¹⁷O a slope of 0.96 and *R*² = 1.00 (Figure 4B).

The previous DFT-GIAO analysis of the shielding tensors in Fe(CO)₅ by Ruiz-Morales et al.¹⁵ focused on the larger deshielding contributions to the parallel tensor component (σ_{33}) in the axial compared to the equatorial positions, both for carbon and for oxygen (cf. Table 1). Their conclusion was that the paramagnetic contributions to σ_{33} are largely due to the coupling of the 2e' highest occupied MO (HOMO) to appropriate $\pi^*(\text{CO})$ -type orbitals by the magnetic vector potential.¹⁵ The

most important virtual MOs in this respect are the 3e'' MO for the equatorial sites and the 3e' MO in the axial sites. Since the 3e' MO in the axial site is lower in energy, the paramagnetic contributions to σ_{33} are larger in the axial site, both for oxygen and for carbon. This in turn leads to the lower isotropic shielding of the axial site.¹⁵ Our own analysis, either fully or partially in terms of canonical MOs, essentially confirms this picture given by Ruiz-Morales et al.

It is, however, more difficult to explain why the shift tensors in the equatorial sites deviate significantly from axial symmetry, an observation made both experimentally and computationally, in particular for oxygen (see Table 1). The calculations clearly show that the behavior of carbon and oxygen differs in this respect. For the equatorial carbon nuclei, the least shielded component, σ_{11} , is oriented parallel to the 3-fold symmetry axis (we will in the following discuss absolute shieldings σ), i.e., $\sigma_{11} = \sigma_{zz}$ (cf. Figure 5A). σ_{22} lies within the equatorial plane, $\sigma_{22} = \sigma_{yy}$, and σ_{33} is generally oriented parallel to the C–O bond, $\sigma_{33} = \sigma_{xx}$. In contrast, for oxygen, $\sigma_{11} = \sigma_{yy}$ but $\sigma_{22} = \sigma_{zz}$. Intuitively, one would expect that these deviations from axial symmetry are connected in some way to back-bonding interactions between metal d_{π} and the appropriate $\pi^*(\text{CO})$ orbitals. However, both the conventional localized (derived from a Boys localization) and canonical MO analyses indicate that many different orbitals contribute in a complex way to the

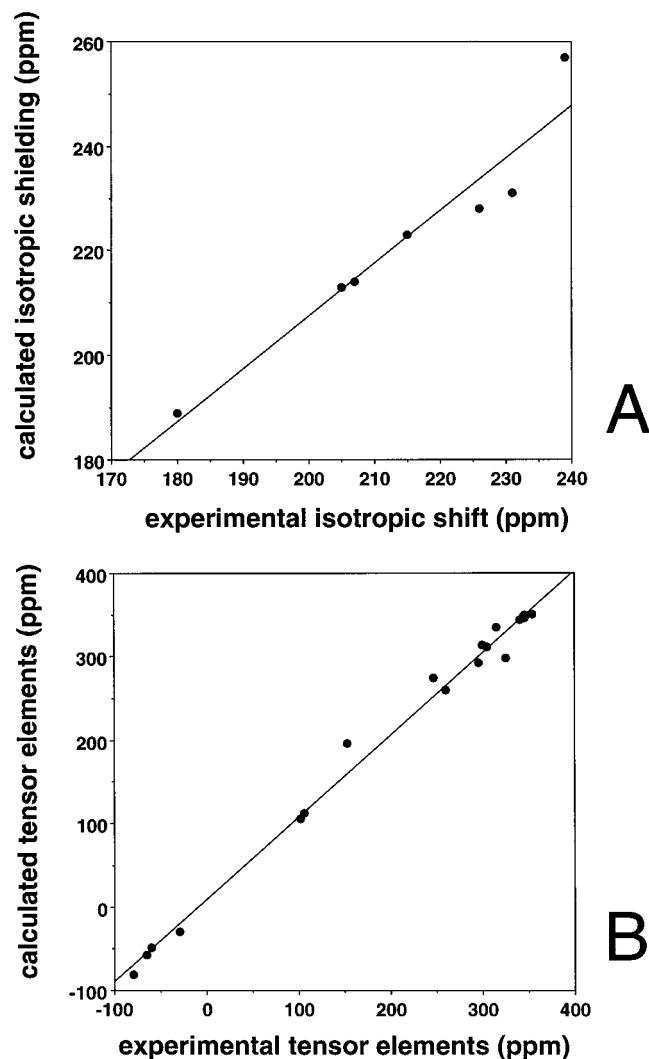


Figure 3. Comparisons between experimental and theoretical ^{13}C shifts and individual shift tensor elements for $\text{Fe}(\text{CO})_5$, $\text{Fe}_2(\text{CO})_9$, $\text{Ni}_2(\eta^5\text{-C}_5\text{H}_5)_2(\text{CO})_2$, and $\text{Rh}_6(\text{CO})_{16}$: (A) isotropic shifts; slope = 0.98, $R^2 = 0.92$; (B) shift tensor elements, slope = 0.99, $R^2 = 1.00$.

differences between σ_{11} and σ_{22} . These analyses do not allow a simple interpretation.

More insight is provided by the IGLO-PM analysis: in the case of the equatorial oxygen shielding tensor, the differences between σ_{zz} and σ_{yy} are now largely concentrated in the contribution from the $\sigma(\text{CO})$ bonding PM-LMO. Table 2 gives a further breakdown of this contribution into individual occupied/virtual couplings within the sum-over-states expression^{23,24} for σ^{p} . It shows that the (canonical) virtual $\pi^*(\text{CO})$ -type MOs important for σ_{yy} (those parallel to the 3-fold axis, π_z^*) are overall lower in energy than those (oriented within the equatorial plane, π_y^*) contributing to σ_{zz} . Moreover, with the $2e''$, $2a_2''$, and $3e''$ MOs, three π_z^* orbitals contribute significantly to σ_{yy} , compared to only two π_y^* MOs ($1a_2'$ and $4e'$) for σ_{zz} . Apparently, back-bonding from metal d-orbitals into $\pi_z^*(\text{CO})$ -type orbitals is somewhat less effective than that into $\pi_y^*(\text{CO})$ -type MOs, leaving the $\pi_z^*(\text{CO})$ -type MOs lower in energy, and thus more accessible to coupling with the $\sigma(\text{CO})$ -type PM-LMO (induced by the magnetic vector potential). It appears that the d_{xz} , d_{yz} metal orbitals best suited for back-bonding interactions with the $\pi_z^*(\text{CO})$ -type MOs are not fully available, since they also contribute to back-bonding into axial $\pi^*(\text{CO})$ orbitals.

For the equatorial carbon shielding tensors, the same $\sigma(\text{CO})$

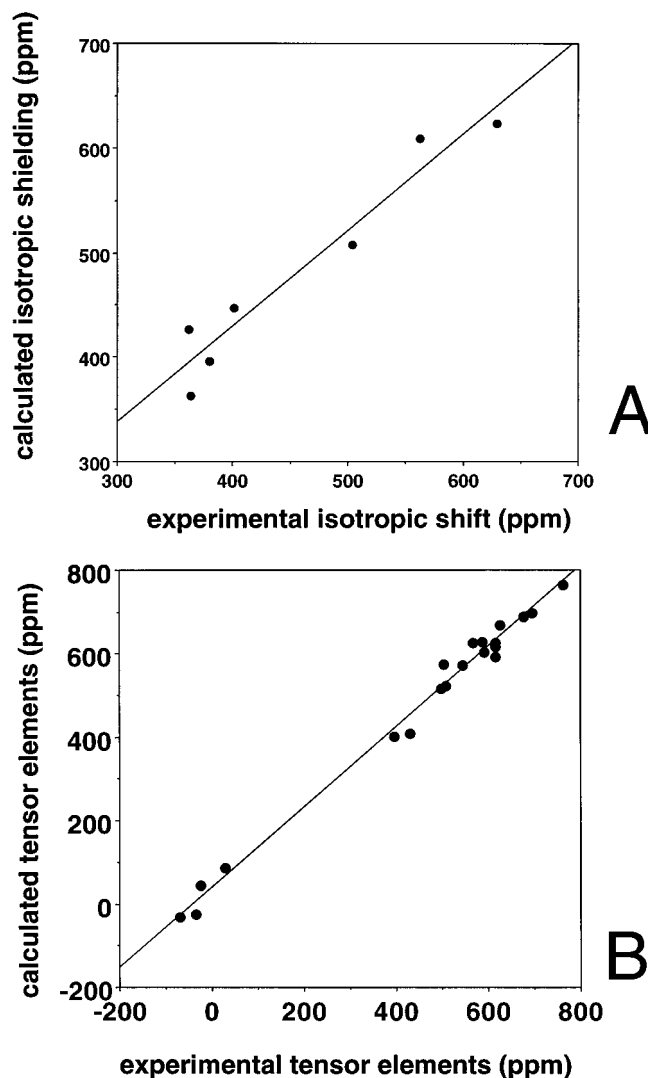


Figure 4. Comparisons between experimental and theoretical ^{17}O shifts and individual shift tensor elements for $\text{Fe}(\text{CO})_5$, $\text{Fe}_2(\text{CO})_9$, $\text{Ni}_2(\eta^5\text{-C}_5\text{H}_5)_2(\text{CO})_2$, and $\text{Rh}_6(\text{CO})_{16}$: (A) isotropic shifts, slope = 0.89, $R^2 = 0.94$; (B) shift tensor elements, slope = 0.96, $R^2 = 1.00$.

PM-LMO obtained in the IGLO-PM procedure also contributes more to σ_{yy} than to σ_{zz} . However, the overall importance of this contribution is only about half of that in the oxygen case (this also holds for the difference between the σ_{zz} and σ_{yy} contributions), and couplings between metal-centered d_{π} -type PM-LMOs and $\sigma^*(\text{Fe}-\text{C})$ type MOs are more important. These are larger for σ_{zz} than for σ_{yy} , leading to the observed orientation and to the smaller deviation from axial symmetry, compared to oxygen.

(b). **$\text{Fe}_2(\text{CO})_9$.** The iron dimer has the structure shown in Figure 5B, in which there are two different types of CO: terminal (μ_1) and bridging (μ_2). Both sites are well resolved in solid-state MAS NMR spectra, as shown in Figure 6, and the principal components of the shielding tensors are reported in Table 1.

For the bridging carbonyls in $\text{Fe}_2(\text{CO})_9$, the ^{17}O results are the first solid-state ^{17}O NMR results to be reported for a μ_2 -CO, and are of some interest since the ^{17}O shifts were already predicted.¹⁷ As may be seen in Table 1 and Figures 3 and 4, there is good agreement between the experimental results and the previous predictions. As expected, the overall breadths of the tensors decrease in a major way on moving from $\mu_1 \rightarrow \mu_2$ M-CO bonding, due to the large deshielding of the parallel

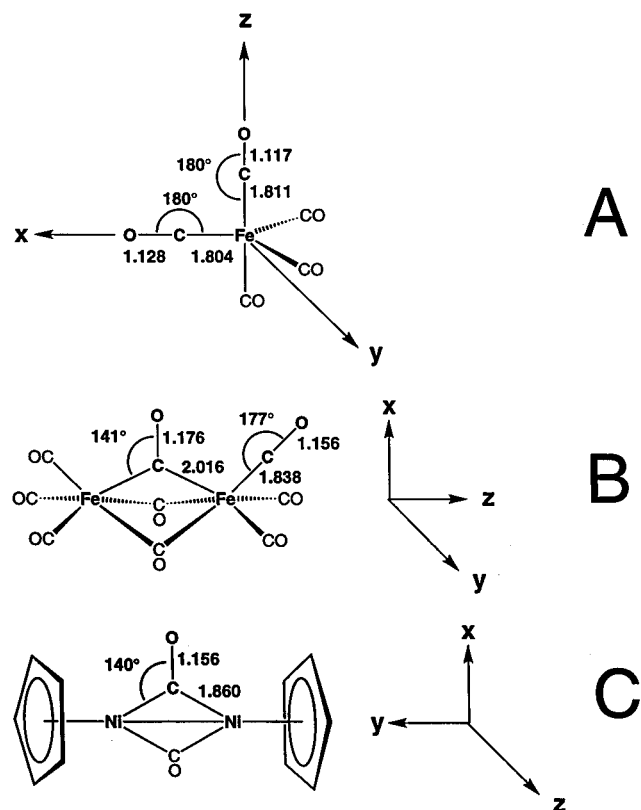


Figure 5. Experimental structures (refs 30–32) of $\text{Fe}(\text{CO})_5$, $\text{Fe}_2(\text{CO})_9$, and $\text{Ni}_2(\eta^5\text{-C}_5\text{H}_5)_2(\text{CO})_2$ showing bond lengths and angles together with the Cartesian coordinate system used for the discussion of the nuclear shielding tensors: (A) $\text{Fe}(\text{CO})_5$; (B) $\text{Fe}_2(\text{CO})_9$; (C) $\text{Ni}_2(\eta^5\text{-C}_5\text{H}_5)_2(\text{CO})_2$.

shielding tensor component for the bridging ligands, which is oriented along the C–O axis.

The most striking computational observation⁴⁶ for $\text{Fe}_2(\text{CO})_9$ is that the largest element, δ_{11} , of the bridging oxygen shift tensor is oriented along the C–O axis ($\delta_{11} = \delta_{xx}$; cf. Figure 5B for the Cartesian coordinates). While this appears unusual for a CO ligand, it is the typical behavior found for organic carbonyl groups.^{47,48} This is due to the fact⁴⁸ that in ketones, aldehydes, amides, etc., the coupling between the oxygen σ lone pair and the carbonyl π^* orbital leads to large deshielding contributions polarized along the C–O axis, which dominate the oxygen shielding (δ_{22} is oriented perpendicular to the C–O bond, but within the molecular plane). For the carbon shielding in organic carbonyl groups, π – π^* and $\sigma(\text{C-X})$ – π^* coupling (X = hydrogen, carbon, nitrogen, etc.) dominates, and thus the parallel component is smaller than the in-plane, perpendicular one. In contrast, for C_{bridge} in $\text{Fe}_2(\text{CO})_9$, δ_{11} is parallel to the Fe–Fe axis ($\delta_{11} = \delta_{zz}$), and δ_{33} is oriented along the C–O axis ($\delta_{33} = \delta_{xx}$). Thus, while the orientation of the bridging oxygen shift tensor in $\text{Fe}_2(\text{CO})_9$ resembles that for an organic carbonyl group, the bridging carbon shift tensor is quite different (also cf. discussion in ref 49).

It is the presence of low-lying $\pi^*(\text{C-O})$ orbitals perpendicular to the $\text{Fe}-(\text{CO})_{\text{bridge}}-\text{Fe}$ plane (π^*_y), in particular the high-lying in-plane bridge-bonding $2e''$ HOMO (see Figure 7 for a

qualitative canonical MO scheme), that controls the appearance of the bridging CO shift tensors. Our previous analysis, in terms of localized orbital contributions, already showed that orbitals localized in the bridge-bonding region are responsible for the large paramagnetic shielding contributions to the parallel tensor component.¹⁷ However, due to the delocalized nature of the bridge bond, the insights provided by the localized MO analysis were limited.

More information is obtained when the $2e''$ HOMO (see Figure 8A and Figure 7) is excluded from the IGLO localization procedure, i.e., it is kept canonical. This is a reasonable approximation, as shown by comparison of this “partial IGLO” with the “full IGLO” shielding results listed in Table 3. This table also shows that the coupling of the HOMO with the appropriate π^*_y -type virtual MO combinations (in particular $2e'$, see Figures 7 and 8A) largely accounts for the deshielding of the ^{17}O shielding tensor element parallel to the C–O bond ($\sigma_{11} = \sigma_{xx}$). While this resembles the situation for ketones/aldehydes to some extent (cf. above), it should be noted that in the latter case it is the coupling of the oxygen π_z lone-pair-type orbitals with the π_y^* MO that has been found to be important.⁴⁸ For the bridging carbon atoms in $\text{Fe}_2(\text{CO})_9$ the paramagnetic contributions caused by $2e'' \rightarrow 2e'$ coupling are also significant, but they are not large enough to change the orientation of the shift tensor, thus leaving $\sigma_{33} = \sigma_{xx}$.

The significant asymmetry ($\sigma_{zz} < \sigma_{yy}$) of the bridging carbon and oxygen shift tensors comes from a variety of occupied orbital contributions (both in canonical or in Boys or PM localized analyses). However, detailed inspection of the different terms in the sum-over-states expression clearly suggests that it is the presence of low-lying π^*_y -type, and the absence of low-lying π^*_z -type, virtual MOs which account for the asymmetry. This is also reminiscent of the situation found with organic carbonyl groups.⁴⁸

The terminal oxygen and carbon shielding/shift tensors are unremarkable, except for the notable asymmetry for oxygen (ca. 25 ppm experimentally, ca. 10 ppm calculated). For both carbon and oxygen, the computed δ_{11} is oriented within the Fe–Fe–C–O plane (xz , cf. Figure 5B), δ_{22} is perpendicular to this plane, and δ_{33} is parallel to the CO axis. While the actual asymmetry is smaller, and its detailed PM-LMO analysis is somewhat more tedious than for the equatorial carbonyl ligands in $\text{Fe}(\text{CO})_5$ (cf. the discussion above), essentially the same conclusions hold as in the previous case. Thus, back-bonding is apparently somewhat less pronounced into the $\pi^*(\text{CO})$ -type orbitals perpendicular to the plane than into those in the plane, resulting in lower-lying out-of-plane π^* MOs.

(c) $\text{Ni}_2(\eta^5\text{-C}_5\text{H}_5)_2(\text{CO})_2$. The nickel dimer is a second system having μ_2 -CO groups. The M–C–O bond angle is essentially the same as that observed in $\text{Fe}_2(\text{CO})_9$, 140° versus 141° , but the M–CO bond length is much shorter in $\text{Ni}_2(\eta^5\text{-C}_5\text{H}_5)_2(\text{CO})_2$, 1.860 versus 2.016 Å.^{31,32} Our experimental and theoretical results are given in Figure 9 and Table 1.

The comparison to the bridging ligands in $\text{Fe}_2(\text{CO})_9$ is of particular interest. From Table 1 we infer that, while the isotropic carbon shifts of the two species are rather similar (somewhat lower for the nickel compound), there are significant differences in the carbon shift tensors. In particular, the parallel component, δ_{33} , in $\text{Ni}_2(\eta^5\text{-C}_5\text{H}_5)_2(\text{CO})_2$ is significantly more shielded than is δ_{33} for the bridging CO ligands in $\text{Fe}_2(\text{CO})_9$, resulting in a much larger anisotropy of the tensor in the Ni_2 system. The orientation of the oxygen shift tensor also differs from that in $\text{Fe}_2(\text{CO})_9$ by having the lowest shift/largest shielding in the parallel component, as usually expected for carbonyl

(46) We had not noted this unexpected feature previously.¹⁶

(47) (a) Vaara, J.; Kaski, J.; Jokisaari, J.; Diehl, P. *J. Phys. Chem. A* **1997**, *101*, 5069–5081. (b) Asakura, T.; Niizawa, Y.; Williamson, M. P. *J. Magn. Reson.* **1992**, *98*, 646–653.

(48) Detailed LMO analyses for H_2CO are given in: Schindler, M.; Kutzelnigg, W. *J. Chem. Phys.* **1982**, *76*, 1919–1933.

(49) Gleeson, J. W.; Vaughan, R. W. *J. Chem. Phys.* **1983**, *78*, 5384–5392.

Table 2. Analysis of the Absolute Shielding Tensor of the Equatorial Oxygen in Fe(CO)₅: Breakdown of the $\sigma(\text{CO})$ PM-LMO Contribution into Individual Couplings to Virtual (canonical) MOs^a

virtual MO no.	label ^b	character	ϵ (au)	oxygen shielding (ppm)			
				$\sigma_{11}(\sigma_{yy})$	$\sigma_{22}(\sigma_{zz})$	$\sigma_{33}(\sigma_{xx})$	σ_{iso}
1, 2	2e''	$\pi^*(\text{CO}_{\text{eq}})_{zz}$	-0.076	-207.0			-69.0
3	3a ₁ '	$\sigma^*(\text{FeC}_{\text{ax}})$ ^c	-0.067				
4, 5	3e'	$\pi^*(\text{CO}_{\text{ax}})$ ^c	-0.061				
6	2a ₂ ''	$\pi^*(\text{CO}_{\text{eq}})_{zz}$	-0.058	-121.4			-40.5
7	1a ₂ '	$\pi^*(\text{CO}_{\text{eq}})_{yy}$	-0.052		-106.3		-35.4
8, 9	4e'	$\pi^*(\text{CO}_{\text{eq}})_{yy}$	-0.044		-260.7		-86.9
10	3a ₂ ''		-0.018				
11, 12	3e''	$\pi^*(\text{CO}_{\text{eq}})_{zz}$	-0.014	-96.7			-32.2
sum				-425.2	-367.0		-264.0
total				-422.3	-361.5	(+22.2) ^d	-253.9

^a From a DFT-IGLO-PM calculation. See Figure 5 for the coordinate axes used. ^b Notation after ref 15. ^c With some additional $\sigma^*(\text{Fe}-\text{C}_{\text{eq}})$ character. ^d Diamagnetic contribution.

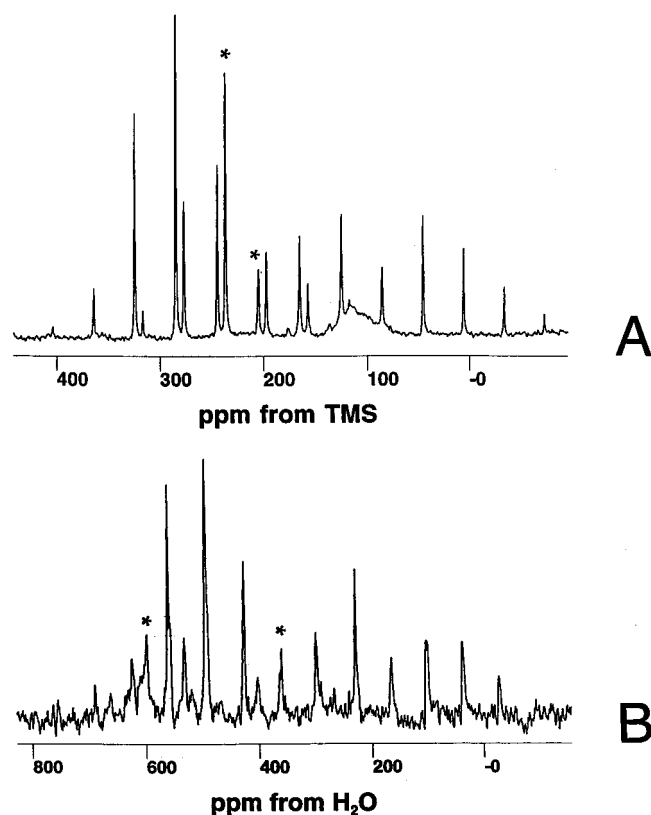


Figure 6. Solid-state MAS NMR spectra of Fe₂(CO)₉ at 296K: (A) 125.6 MHz ¹³C spectrum, spinning speed = 5000 ± 10 Hz, 200 scans at a recycle time of 50 s, 50 Hz line broadening due to exponential multiplication. B; 67.8 MHz ¹⁷O spectrum, spinning speed = 4400 ± 10 Hz, 400 scans at a recycle time of 50 s, 100 Hz line broadening. The centerbands are indicated with an asterisk.

ligands. Thus, while there are obviously large paramagnetic contributions to the parallel component, resulting in a very low anisotropy, they are not quite large enough to change the orientation of the bridging oxygen shift tensor in the way discussed above for Fe₂(CO)₉.

The average of the perpendicular components of the carbon and oxygen shift tensors for the two systems is similar. However, the asymmetry of the oxygen shift tensor is notably larger for the Fe₂ system, both experimentally and computationally. The same holds also for the computed carbon shift tensors (here the experimental asymmetries would be of comparable size, but this might be an artifact due to difficulties in determining δ_{22}).

The analysis of the shielding tensors for Ni₂(η^5 -C₅H₅)₂(CO)₂

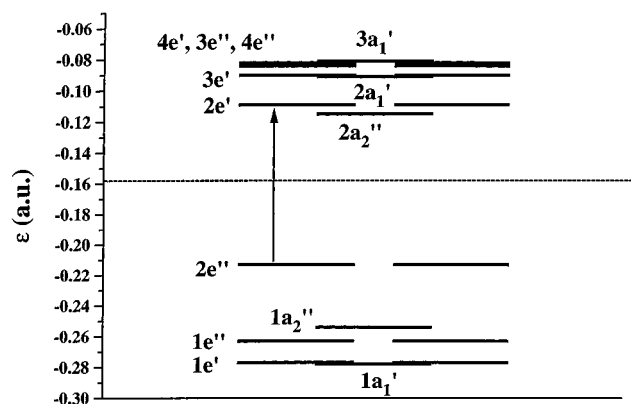


Figure 7. Frontier MO diagram for Fe₂(CO)₉, with orbital energies from the present DFT calculations. Numbering of levels starts arbitrarily at the lowest orbital shown, for each symmetry.

is somewhat more complicated than for the iron system, due to the lower molecular symmetry. While the “real system”, i.e., the experimental structure used for the computations, features no symmetry at all, we may for interpretation purposes (symmetry labeling of the orbitals) think of a structure idealized to C_{2v} symmetry (see Figure 5C). A straightforward interpretation of the shielding tensors is then obtained when the four highest occupied MOs (“1b₂”, “1a₁”, “1a₂”, “2b₂”) are excluded from localization in a “partial IGLO” analysis (Table 4, see Table 5 for a characterization of the frontier MOs).

Table 4 shows that the deshielding contributions to σ_{33} (for both carbon and oxygen) come largely from the bridge-bonding “1a₂” MO, which has large in-plane $\pi^*_y(\text{CO})$ character (see Table 5, and Figure 5C for the Cartesian axes), and is thus somewhat similar to one component of the 2e'' HOMO in Fe₂(CO)₉, described above. Some additional contributions arise from the “2b₂” HOMO (which also has some in-plane $\pi^*_y(\text{CO})$ character, but with smaller coefficients), and from remaining metal AO-like LMOs. A more detailed inspection of the individual sum-over-states terms of the paramagnetic contributions indicates that coupling of the two highest occupied MOs (“1a₂”, “1b₂”) to the unoccupied “2a₁” and “2b₁” MOs dominates σ_{33} . The two virtual MOs have large out-of-plane $\pi^*_z(\text{CO})$ character. Thus, the overall picture leading to deshielding of the parallel component of the bridging oxygen and carbon shielding tensors is closely related to the analysis described above for Fe₂(CO)₉. The main differences appear to be the larger orbital energy differences (computed to be 0.12 eV for the “1a₂”-“2a₁” coupling, 0.15 eV for the “1a₂”-“2b₁” cou-

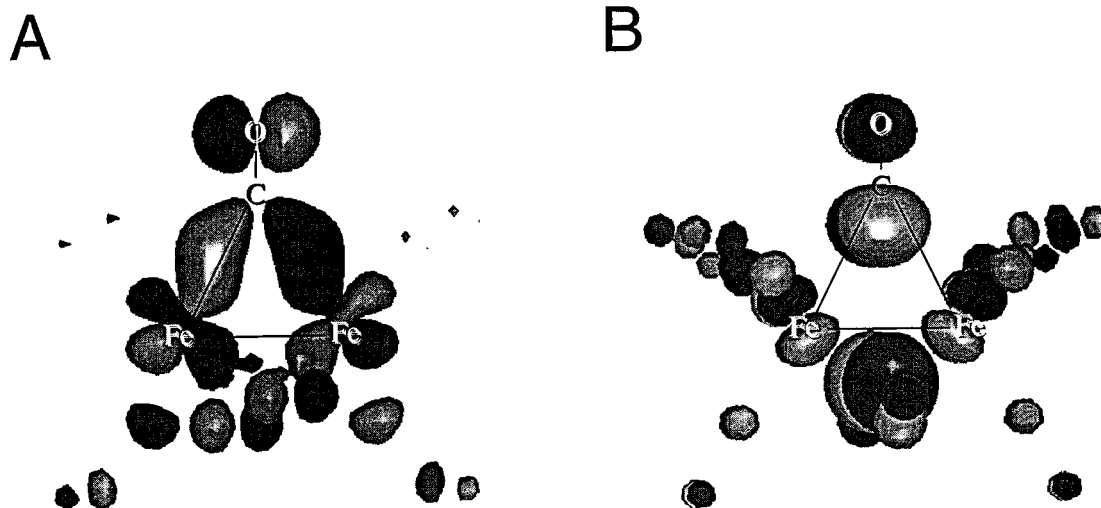


Figure 8. Isosurface representation (isosurfaces for ± 0.05 au) of one of each of the two orbitals belonging to the $2e''$ HOMO set (A) and to the virtual $2e'$ MO set in $\text{Fe}_2(\text{CO})_9$ (B).

Table 3. Combined MO/LMO Analysis of ^{13}C and ^{17}O Absolute Shielding Tensors for Bridging Carbonyl Ligands in $\text{Fe}_2(\text{CO})_9^a$

MO/LMO	σ_{iso}	σ_{zz}	σ_{yy}	σ_{xx}
(a) carbon				
1s(C) LMO	+200.0	+200.0	+200.0	+200.0
LP(O) LMO	-30.2	-58.1	-35.6	+3.3
C \equiv O LMOs	-46.6	-100.4	-75.7	+35.9
$\sigma(\text{Fe}-\text{C})$ LMO	-93.8	-147.0	-157.0	22.6
$\Sigma\text{AO}(\text{Fe})$ LMOs	-23.9	-24.9	-23.8	-23.4
$2e''$ MO	-80.9	+0.7	+18.6	-262.0
sum ^b	-75.4	-129.7	-73.5	-23.6
total ^c	-72.8	-126.4	-70.5	-21.7
“full-IGLO” ^d	-69.1	-126.4	-71.8	-8.8
(b) oxygen				
1s(O) LMO	+270.2	+270.2	+270.2	+270.2
LP(O) LMO	-71.0	-215.0	-33.3	+35.4
C \equiv O LMOs	-84.2	-112.1	-143.7	+3.2
$\sigma(\text{Fe}-\text{C})$ LMO	-161.1	-304.1	-300.4	+121.0
$\Sigma\text{AO}(\text{Fe})$ LMOs	-27.9	-29.0	-24.7	-29.9
$2e''$ MO	-241.5	+2.9	+150.6	-879.5
sum ^b	-315.5	-387.1	-81.3	-479.8
total ^c	-324.5	-390.2	-86.0	-497.3
“full-IGLO” ^d	-315.7	-388.8	-100.0	-458.1

^a From “partial IGLO” calculations with the $2e''$ HOMO excluded from the Boys localization. See Figure 5B for the Cartesian axes. Notation: LP = lone pair, $\Sigma\text{AO}(\text{Fe})$ = sum of metal AO-like LMO contributions (only individual contributions with one element > 3 ppm for carbon and > 5 ppm for oxygen have been summed up). ^b Sum of all listed contributions. ^c Sum of all contributions. ^d Average over all three bridging ligands.

pling⁵⁰) when compared to the iron compound (computed to be 0.10 eV for the $2e''$ - $2e'$ coupling). This in turn is probably related to the fact that the much more compact metal d-orbitals in $\text{Ni}_2(\eta^5\text{-C}_5\text{H}_5)_2(\text{CO})_2$ are less involved in back-bonding to the bridging carbonyl ligands than are the more extended ones in $\text{Fe}_2(\text{CO})_9$.

Experimentally, the asymmetries $|\sigma_{22} - \sigma_{11}|$ of the bridging carbon and oxygen shielding tensors in the nickel compound (79 and 93 ppm, respectively) are somewhat larger than those of $\text{Fe}_2(\text{CO})_9$ (50 and 67 ppm, cf. Table 1). The computed values agree well with experiment for the iron dimer, but are

(50) Note that these Kohn-Sham orbital energy differences are expected to significantly underestimate the true excitation energies.

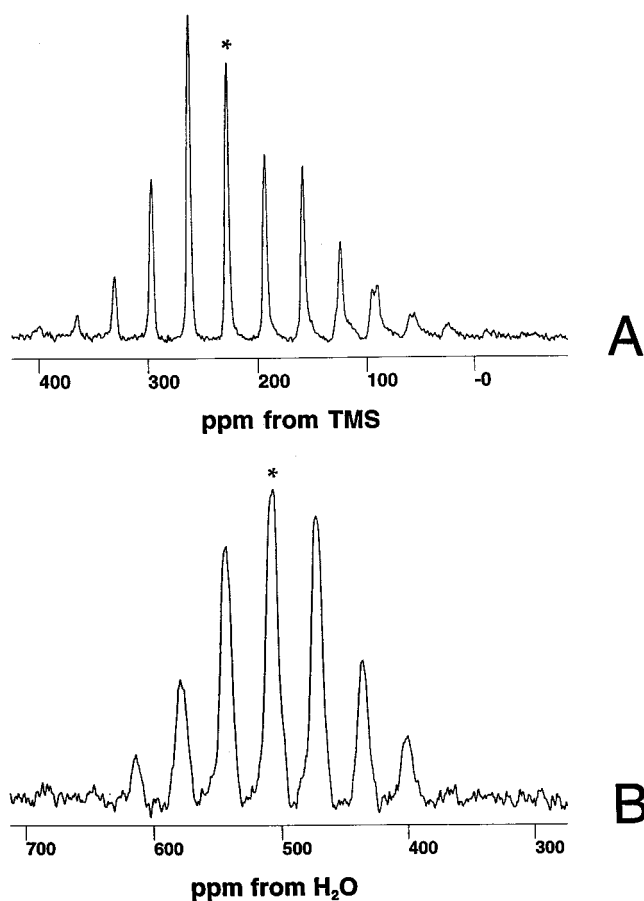


Figure 9. Carbon-13 and oxygen-17 MAS NMR spectra of $\text{Ni}_2(\eta^5\text{-C}_5\text{H}_5)_2(\text{CO})_2$: (A) 125.6 MHz ^{13}C CP-MAS NMR spectrum, spinning speed = 4300 ± 10 Hz, 200 scans, 10 s recycle time, 3 ms CP mix time, 100 Hz line broadening due to exponential multiplication; (B) 67.8 MHz ^{17}O spectrum, spinning speed = 2400 ± 10 Hz, 10 000 scans, 10 s recycle time, in the presence of ^1H decoupling, 100 Hz line broadening. The centerband is indicated with an asterisk.

significantly lower than experiment in the nickel system. While this difference may partly be due to experimental inaccuracies (δ_{22} is generally the most difficult component to determine), some errors may also arise from the IGLO localization procedure in the calculations. For example, an IGLO-PM calculation gives asymmetry values of ca. 15 and 80 ppm for carbon and oxygen,

Table 4. Combined MO/LMO Analysis of ^{13}C and ^{17}O Absolute Shielding Tensors for Bridging Carbonyl Ligands in $\text{Ni}_2(\eta^5\text{-C}_5\text{H}_5)_2(\text{CO})_2^a$

MO/LMO	σ_{iso}	σ_{11}	σ_{22}	σ_{33}
(a) carbon				
1s(C) LMO	+200.0	+200.0	+200.0	+200.0
LP(O) LMO	-28.8	-50.3	-38.4	+2.4
C≡O LMOs	-48.4	-109.3	-77.1	-43.2
$\sigma(\text{Ni}-\text{C})$ LMO	-85.2	-120.5	-155.1	+19.9
$\Sigma\text{AO}(\text{Ni})$ LMOs	-31.3	-14.8	-23.6	-55.9
"1b ₂ MO"	+1.7	+0.7	+9.8	-5.5
"1a ₁ MO"	-7.0	-17.3	+1.1	-4.7
"1a ₂ MO"	-34.5	+0.2	-9.4	-94.4
"2b ₂ MO" (HOMO)	-6.3	+1.2	+1.1	-21.1
sum ^b	-39.8	-110.1	-91.6	+83.8
total ^c	-43.0	-109.9	-92.9	+73.9
"full-IGLO" ^d	-45.0	-108.0	-101.5	+74.7
(b) oxygen				
1s(C) LMO	+270.1	+270.1	+270.1	+270.1
LP(O) LMO	-66.7	-148.9	-86.3	+35.1
C≡O LMOs	-144.6	-247.1	-282.1	+95.6
$\sigma(\text{Ni}-\text{C})$ LMO	-78.2	-100.3	-137.3	+3.3
$\Sigma\text{AO}(\text{Ni})$ LMOs	-41.6	-12.5	-14.4	-102.6
"1b ₂ MO"	-1.4	+0.1	+4.4	-8.5
"1a ₁ MO"	-14.2	-53.6	-8.1	+19.0
"1a ₂ MO"	-59.5	+1.3	+25.2	-325.0
"2b ₂ MO" (HOMO)	-18.2	+0.3	+32.3	-87.2
sum ^b	-194.3	-290.6	-196.6	-100.2
total ^c	-200.3	-290.5	-202.0	-108.3
"full-IGLO" ^d	-199.1	-292.3	-227.0	-77.9

^a From "partial IGLO" calculation with the four highest occupied MOs excluded from the Boys localization. See Figure 5C for the Cartesian axes used. Notation: LP = lone pair, $\Sigma\text{AO}(\text{Ni})$ = sum of metal AO-like LMO contributions (only individual contributions with one element >3 ppm for carbon and >5 ppm for oxygen have been summed up). ^b Sum of all listed contributions. ^c Sum of all contributions. ^d Average over both bridging ligands.

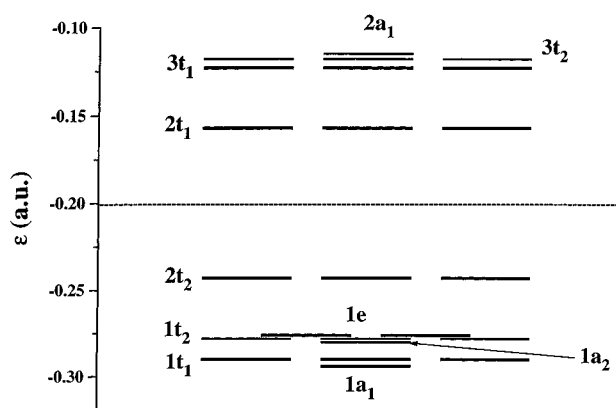
Table 5. Characterization of the Frontier Orbitals of $\text{Ni}_2(\eta^5\text{-C}_5\text{H}_5)_2(\text{CO})_2^a$

	symmetry label ^b	ϵ (au)	character wrt CO	metal character ^c
HOMO-3	1b ₂	-0.207		y^2, z^2
HOMO-2	1a ₁	-0.202	π^*_z	z, yz, y^2, z^2
HOMO-1	1a ₂	-0.185	π^*_y	x, xy
HOMO	2b ₂	-0.160	π^*_y	s, y, yz, z^2
LUMO	1b ₁	-0.098	σ^*	x, xy
LUMO+1	3b ₂	-0.073	π^*_y	x^2, y^2
LUMO+2	2a ₁	-0.063	π^*_z	z, yz, x^2, z^2
LUMO+3	2b ₁	-0.033	π^*_z	xz
LUMO+4	2a ₂	-0.032	π^*_y	x, xy

^a Orbitals from the present DFT calculations. See Figure 5C for the Cartesian axes used. ^b Labels idealized to C_{2v} symmetry. ^c Major metal AO contributions to a given MO with p orbitals denoted x, y, z , and d orbitals as $xy, xz, yz, x^2, y^2, z^2$ (six Cartesian d functions were employed).

respectively, compared to 7 and 64 ppm obtained from the regular IGLO procedure.

The origin of the asymmetry may best be investigated via an IGLO-PM analysis. This gives a large asymmetry in the contribution from a $\sigma(\text{CO})$ -type PM-LMO. Further analysis (in the same manner as discussed above for $\text{Fe}(\text{CO})_5$) then indicates that the coupling of this PM-LMO with the out-of-plane $\pi^*_z(\text{CO})$ -type "2a₁" and "2b₁" virtual (canonical) MOs contributes more deshielding to σ_{11} than the coupling with the in-plane $\pi^*_y(\text{CO})$ -type "3b₂" and "2a₂" MOs to σ_{22} (cf. Table 5).

**Figure 10.** Frontier MO diagram for $\text{Rh}_6(\text{CO})_{16}$, with orbital energies from the present DFT calculations. Numbering of levels starts arbitrarily at the lowest orbital shown, for each symmetry.

Consequently, the origin of the asymmetry is similar to that discussed above for the bridging ligand atoms in $\text{Fe}_2(\text{CO})_9$.

We note here in passing that inspection of the electron localization function (ELF⁵¹) for $\text{Ni}_2(\eta^5\text{-C}_5\text{H}_5)_2(\text{CO})_2$ indicates no direct metal-metal bonding, as discussed previously for $\text{Fe}_2(\text{CO})_9$.¹⁷ Therefore, the overall picture emerging for the electronic structure of the nickel system in comparison with $\text{Fe}_2(\text{CO})_9$ is that the same type of delocalized synergistic $\sigma(\text{CO})$ to metal donor, metal to in-plane $\pi^*(\text{CO})$ acceptor bonding dominates the bridge bond in both species. However, due to the more compact metal d orbitals in the nickel compound, the back-bonding is considerably less pronounced in this system.

(d) $\text{Rh}_6(\text{CO})_{16}$. The rhodium cluster is of interest since its ^{13}C NMR spectrum has been described,^{7,49} and predictions for ^{17}O shieldings have been made previously.¹⁷ The $\text{Rh}_6(\text{CO})_{16}$ molecule has a complex structure containing both μ_1 and μ_3 ligands, as shown above. We obtained both ^{13}C and ^{17}O MAS NMR spectra (data not shown), and deduced the principal components of the shielding tensors as described above. Results are given in Table 1 and Figures 3 and 4, indicating again the good agreement between DFT predictions and experiment.

Our previous DFT-IGLO analysis¹⁷ of the bridging carbon and oxygen shielding tensors in $\text{Rh}_6(\text{CO})_{16}$ indicated that the low anisotropy values and the large isotropic shifts in the bridging position were due to deshielding contributions to the parallel tensor component, σ_{33} , from largely metal-centered LMOs. Further insight was prevented by the fact that the LMOs for this delocalized system partially break the symmetry and are difficult to analyze in chemical terms (see also the discussion above for $\text{Fe}_2(\text{CO})_9$).

A better understanding is again provided by a combined MO/LMO analysis obtained in a "partial IGLO" procedure, keeping the two highest occupied molecular orbitals canonical (1e, 2t₂, see Figure 10; these cluster-bonding MOs have significant $\pi^*(\text{CO}_{\text{bridge}})$ character). The resulting breakdown of the bridging carbon and oxygen shielding tensors is given in Table 6. In both cases, the 2t₂ HOMO makes the largest deshielding contribution to σ_{33} . The 1e MO contribution is significant for oxygen, but relatively small for carbon. In contrast, contributions from remaining metal AO-like LMOs make larger contributions for carbon than for oxygen. As discussed above for $\text{Fe}_2(\text{CO})_9$ and $\text{Ni}_2(\eta^5\text{-C}_5\text{H}_5)_2(\text{CO})_2$, the overall deshielding contributions to the parallel tensor component are again considerably more pronounced for oxygen than for carbon. As

(51) See, e.g.: Savin, A.; Becke, A. D.; Flad, J.; Nesper, R.; von Schnering, H. G. *Angew. Chem.* **1991**, *103*, 421-424; *Angew. Chem., Int. Ed. Engl.* **1991**, *30*, 409-412.

Table 6. Combined MO/LMO Analysis of ^{13}C and ^{17}O Absolute Shielding Tensors for Bridging Carbonyl Ligands in $\text{Rh}_6(\text{CO})_{16}$ ^a

MO/LMO	σ_{iso}	$\sigma_{11} = \sigma_{22}$	σ_{33}
(a) carbon			
1s(C) LMO	+200.0	+200.0	+200.0
LP(O) LMO	-71.8	-118.3	21.3
C≡O LMOs	-57.7	-100.7	28.4
LP(C) LMO	-23.3	-36.6	3.4
$\Sigma\text{AO}(\text{Rh})$ LMOs	-16.6	+1.4	-53.2
1e MO	-9.0	-10.2	-7.3
2t ₂ MO	-53.4	-37.5	-85.1
sum ^b	-31.8	-102.0	+107.5
total ^c	-27.2	-93.3	+105.3
“full-IGLO”	-43.3	-105.7	+81.5
(b) oxygen			
1s(O) LMO	+270.0	+270.0	+270.0
LP(O) LMO	-12.1	-35.9	+35.6
C≡O LMOs	-151.3	-321.2	+3.7
LP(C) LMO	-159.5	-241.2	+188.5
$\Sigma\text{AO}(\text{Rh})$ LMOs	-14.0	+5.2	-52.2
1e MO	-79.2	-63.3	-110.9
2t ₂ MO	-130.1	+80.4	-551.2
sum ^b	-276.2	-306.0	-216.5
total ^c	-302.2	-322.2	-262.1
“full-IGLO”	-301.3	-318.3	-267.1

^a From “partial IGLO” calculation with the 1e and 2t₂ MOs (HOMO-1, HOMO, see Figure 10) excluded from the Boys localization. Notation: LP = lone pair (LP(C) corresponds to the LMO pointing toward the center of the bridged Rh₃ face), $\Sigma\text{AO}(\text{Rh})$ = sum of metal AO-like LMO contributions (only individual contributions with one element > 3 ppm for carbon and > 5 ppm for oxygen have been summed up). ^b Sum of all listed contributions. ^c Sum of all contributions.

a result, the oxygen shielding anisotropy almost vanishes. However, in contrast to the bridging carbonyl ^{17}O shielding tensor of $\text{Fe}_2(\text{CO})_9$ (cf. above), the parallel tensor component is still the most shielded one, σ_{33} . A further breakdown of the 2t₂ and 1e contributions to σ_{33} indicates strong couplings, particularly with the 2t₁ and 3t₁ MOs (Figure 10, these also have significant $\pi^*(\text{CO}_{\text{bridge}})$ character) and to some other MOs at higher energies. The shielding tensors computed with the “partial IGLO” procedure agree reasonably well with the “full IGLO” results and with experiment, which gives us confidence in this refined MO/LMO interpretation.

The shielding tensors for the terminal carbonyl ligands are not required by symmetry to be axially symmetric, and do indeed deviate somewhat from axial symmetry, particularly for oxygen (cf. Table 1). For both carbon and oxygen, σ_{11} is perpendicular to a plane containing the midpoint of the Rh₆ octahedron and both ligand atoms, and σ_{22} is oriented in-plane. A detailed analysis is difficult, since even in an IGLO-PM analysis, the asymmetry is distributed over a considerable number of PM-LMOs. It is to be expected, however, that the asymmetry is connected to slight differences in the back-bonding between metal d_π-type orbitals and the out-of-plane and in-plane $\pi^*(\text{CO}_{\text{terminal}})$ -type MOs, as described above for $\text{Fe}(\text{CO})_5$.

^{17}O Nuclear Quadrupole Couplings. Finally, we investigated the nuclear quadrupole coupling constants (NQCC) in the four systems of interest. Typical nutation⁵² results are given in Figure 11. The result on $\text{Ni}_2(\eta^5\text{-C}_5\text{H}_5)_2(\text{CO})_2$ yields an NQCC value of 1.80 MHz, from the nutation simulation shown in Figure 11. For $\text{Fe}_2(\text{CO})_9$, Figure 9B, we find an NQCC = 3.30 MHz for the bridging oxygen. These results, and those

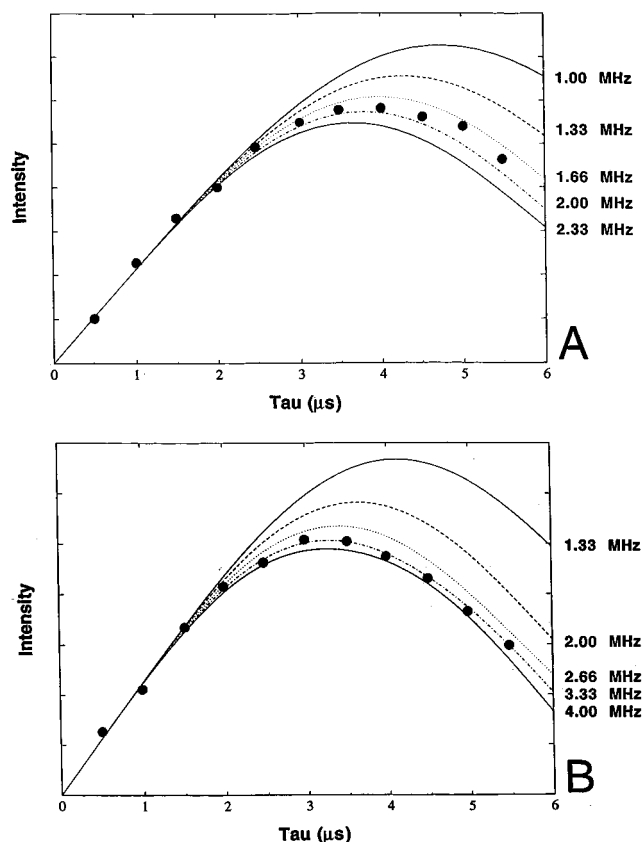


Figure 11. Representative results showing the evaluation of ^{17}O NQCC values for $\text{Ni}_2(\eta^5\text{-C}_5\text{H}_5)_2(\text{CO})_2$ and $\text{Fe}_2(\text{CO})_9$. (A) Nutation results (●) and five nutation simulations for $\text{Ni}_2(\eta^5\text{-C}_5\text{H}_5)_2(\text{CO})_2$, using a γH_1 corresponding to a 90°(solution) pulse width of 9.6 μs . η was taken to be 0 in the simulation. (B) Same as A but for the bridging carbonyl in $\text{Fe}_2(\text{CO})_9$ and a 90°(solution) pulse width of 9.0 μs .

for the other compounds investigated, are given in Table 7, together with the theoretical predictions. Here, note that the signs for the experimental values are given in parentheses, and have been inferred from the results of the calculations (see below). Figure 12 shows that, using these signs, there is an excellent correlation between theory and experiment, with a slope of 1.03, a R^2 value of 0.959, and an intercept of only 0.13 MHz. In addition, the rms error from the fitted line is only 0.37 MHz, which is about the magnitude of the error on the experimental NQCC determinations (and in most cases the uncertainty in η , the efg asymmetry parameter).

Since there is clearly quite good agreement between computed and experimental ^{17}O NQCC's (cf. Table 7), it appeared worthwhile to have a closer look at the computed NQC tensors, relating them to the bonding in these carbonyl complexes and clusters. Table 7 characterizes the individual principal components of the NQC tensors in terms of their orientation with respect to the carbonyl ligand atomic positions. We have also included the free CO molecule and a typical terminal carbonyl ligand, CO in $\text{Cr}(\text{CO})_6$, for purposes of comparison.

In free carbon monoxide, the NQCC is computed to be 4.07 MHz (cf. the experimental value of 4.34 MHz⁵³), with q_{11} being positive and oriented along the CO axis. In going to a typical axially symmetric terminal coordination position, as with the CO ligands in $\text{Cr}(\text{CO})_6$ (experimental NQCC < 1 MHz⁹) or the axial ligands in $\text{Fe}(\text{CO})_5$, the orientation and sign of the electric field gradient remain the same, but the apparent NQCC

(52) Freude, D.; Haase J. In *NMR Basic Principles and Progress*; Fluck, E., Günther, H., Kosfeld, R., Seelig, J., Eds.; Springer-Verlag: Berlin, 1993; Vol. 29, pp 3–90.

(53) Frerking, M. A.; Langer, W. D. *J. Chem. Phys.* **1981**, *74*, 6990–6991.

Table 7. Principal Components of Computed Carbonyl ^{17}O NQC Tensors Together with a Characterization of Their Orientation, Compared to Experimental NQCCs

compd	nucleus	e^2qQ/h (MHz, exptl)	q_{11}	q_{22}	q_{33}
CO^a		(+) 4.34 ^b	+4.07 (q_{\parallel})	-2.04 (q_{\perp})	-2.04 (q_{\perp})
$\text{Cr}(\text{CO})_6^a$		$\leq 1^c$	+1.36 (q_{\parallel})	-0.68 (q_{\perp})	-0.68 (q_{\perp})
$\text{Fe}(\text{CO})_5^d$	O_{axial}	(+) 1.17	+1.80 (q_{\parallel})	-0.90 (q_{\perp})	-0.90 (q_{\perp})
	$\text{O}_{\text{equatorial}}$	(-) 1.87	-1.97 (q_{\perp} ; q_z)	+1.62 (q_{\parallel} ; x)	+0.35 (q_{\perp} ; y)
$\text{Fe}_2(\text{CO})_9^e$	$\text{O}_{\text{terminal}}$	(+) 1.60	+1.25 (q_{\parallel} ; x, z)	-0.76 (q_{\perp} ; $-x, z$)	-0.49 (q_{\perp} ; y)
	O_{bridge}	(+) 3.30	+4.20 (q_{\perp} ; z)	-3.81 (q_{\parallel} ; x)	-0.39 (q_{\parallel} ; y)
$\text{Ni}_2(\eta^5\text{-C}_5\text{H}_5)_2(\text{CO})_2^f$	O_{bridge}	(-) 1.80	-1.57 (q_{\perp} ; z)	+1.50 (q_{\parallel} ; x)	+0.07 (q_{\perp} ; y)
	$\text{O}_{\text{terminal}}$	(+) 1.20	+0.89 (q_{\parallel})	-0.74 (q_{\perp} ; out-of-plane ^g)	-0.15 (q_{\perp} ; in-plane ^g)
$\text{Rh}_6(\text{CO})_{16}$	$\text{O}_{\text{terminal}}$	(+) 1.20	+0.89 (q_{\parallel})	-0.74 (q_{\perp})	-0.15 (q_{\perp})
	O_{bridge}	(-) 0.89	-0.75 (q_{\parallel})	+0.37 (q_{\perp})	+0.37 (q_{\perp})

^a Computed at the same level (with IGLO-II basis on C and O) as the other systems in this study. ^b Cf. ref 54. ^c Cf. ref 9. ^d See Figure 5A for Cartesian axes. ^e See Figure 5B for Cartesian axes. ^f See Figure 5C for Cartesian axes. ^g Out-of-plane and in-plane refer to a symmetry plane containing the midpoint of the Rh_6 octahedron and the terminal carbonyl ligand of interest.

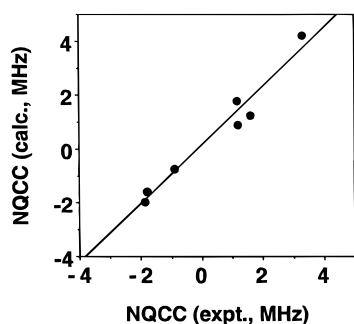


Figure 12. Correlation between the experimentally determined ^{17}O NQCC values found in $\text{Fe}(\text{CO})_5$, $\text{Fe}_2(\text{CO})_9$, $\text{Ni}_2(\eta^5\text{-C}_5\text{H}_5)_2(\text{CO})_2$, and $\text{Rh}_6(\text{CO})_{16}$ and those computed by density functional theory. Data taken from Table 7. Slope = 1.09, $R^2 = 0.959$, intercept = 0.13 MHz, rmsd from the fitted line = 0.37 MHz.

is reduced by a factor of about 2 or 3. It is very tempting to ascribe this “coordination shift” of the ^{17}O NQCC to back-bonding into $\pi^*(\text{CO})$ orbitals in the complexes. However, inspection of canonical MO and nuclear contributions to the NQC tensor elements show very little change in the contributions from π -type MOs upon coordination, and in fact the “coordination shift” appears to be largely due to changes in the contributions from σ -type MOs, and from the additional (metal and other ligand) nuclei.

The NQC tensors for the terminal ligands in $\text{Fe}_2(\text{CO})_9$ and $\text{Rh}_6(\text{CO})_{16}$ are similar to those in the above “typical terminal ligand” bonding situations. The only difference is that the axial symmetry of the tensor is lost (cf. the shielding tensor discussions above), i.e., $|q_{22}| > |q_{33}|$. For $\text{Fe}_2(\text{CO})_9$, q_{22} lies within the Fe–C–O plane, while q_{33} is out-of-plane. In contrast, for $\text{Rh}_6(\text{CO})_9$, q_{22} is perpendicular to the plane containing the midpoint of the Rh_6 octahedron and both ligand atoms, with q_{33} being in-plane.

A rather different picture applies to the equatorial oxygen nuclei in $\text{Fe}(\text{CO})_5$. Here, the component of the NQC tensor perpendicular to the CO axis (but parallel to the 3-fold axis) is so negative that it determines the sign of the NQCC. In contrast, the parallel component ($q_{22} = +1.62$ MHz) is still comparable to those for the other terminal ligands investigated. A detailed breakdown of the NQC tensors in these complexes and clusters is complicated by the fact that many different canonical orbitals,

as well as many of the nuclei in the system, contribute significantly to the electric field gradients. Nevertheless, some idea of the origin of the significant asymmetry of the NQC tensor for the equatorial oxygens in $\text{Fe}(\text{CO})_5$ (cf. the asymmetry of the shielding tensor discussed above) may still be obtained: negative contributions to q_{11} (q_{zz}) but positive contributions to q_{33} (q_{yy}) come from all those occupied orbitals with significant $\pi_x(\text{CO})$ and $\pi_y^*(\text{CO})$ (for the HOMO) character, i.e., from MOs of e' and a_2' symmetry. A sum of these terms gives a -11.54 MHz contribution to q_{11} and a $+14.29$ MHz contribution to q_{33} . In contrast, MOs with significant $\pi_z(\text{CO})$ and $\pi_z^*(\text{CO})$ character (e'' and a_2'' MOs) contribute positively (overall $+16.20$ MHz) to q_{11} and negatively (-8.46 MHz) to q_{33} . Summing up these e' , a_2' , e'' , and a_2'' contributions, we obtain $+4.66$ MHz for q_{11} and $+5.83$ MHz for q_{33} . The resulting asymmetry of 1.17 MHz has to be compared to the overall electronic contributions to q_{11} and q_{33} of -3.23 and -2.26 MHz, respectively, i.e., to an asymmetry of 0.97 MHz. Thus, the unequal population of MOs with π_z (and π_z^*) and π_y (and π_y^*) character dominates the differences between the two perpendicular components of the NQC. Consequently, the NQC tensor does indeed reflect to some extent the unsymmetrical π back-bonding to the equatorial ligands, albeit in a different way than for the shielding tensors.

For the bridging ligands in $\text{Fe}_2(\text{CO})_9$, the relatively large oxygen NQCC is determined by the (positive) perpendicular NQC tensor element in the z direction (i.e. parallel to the Fe–Fe axis, cf. Figure 5B). In contrast, the bridging oxygen NQCC in the nickel complex is determined by the (negative) out-of-plane perpendicular contribution. Obviously, the differences in bonding for doubly bridging vs terminal positions, as well as between the two different dimers, is reflected strongly in these NQC tensors.

The detailed MO analysis of the NQC tensors for the larger systems becomes increasingly cumbersome, due to the large number of MO and nuclear contributions to be considered. We thus restrict our discussion to a brief remark on the bridging CO ligands in $\text{Rh}_6(\text{CO})_{16}$. As shown in Table 7, the orientation is the same, but the signs of all contributions are the reverse of those which are found in “typical” terminal ligands, such as in $\text{Cr}(\text{CO})_6$. Inspection of the MO and nuclear contributions indicates that this is not due to the nuclear potential, but to larger

contributions (negative to q_{11} , positive to q_{22} and q_{33}) from π -type MOs in the bridging compared with the terminal positions. While it is again tempting to ascribe this to the much larger back-bonding in the bridging position, the analysis does not appear to allow this connection to be made unambiguously, although population analyses do of course clearly confirm the larger back-bonding.

Conclusions

The present study represents the first detailed solid-state NMR investigation of both ^{13}C and ^{17}O chemical shifts, chemical shift tensor elements, and ^{17}O nuclear quadrupole coupling constants, in a variety of metal carbonyls containing μ_1 -, μ_2 -, and μ_3 -CO ligands, supplemented by extensive quantum chemical (DFT) calculations.

The accuracy of DFT methods for the computation of ligand chemical shieldings/shift tensors in transition-metal complexes and clusters has now progressed to the stage where detailed comparisons with shifts and individual tensor elements obtained by solid-state NMR spectroscopy can be made. Since the computations are relatively straightforward and fast even for medium-sized systems, they provide an efficient prescreening for the sometimes demanding experimental studies. Such a combination of theoretical and solid-state NMR approaches may now begin to be used as a means for structure elucidation, e.g., in cases where decisions between different models need to be made. As indicated already in the Introduction, many possible areas of chemistry may benefit from this type of approach, including the fascinating field of transition-metal compounds in biochemistry.⁵⁴

However, the calculations provide even more insight than this since they give the orientation of the shift tensors with respect to the molecular framework, information that is difficult to obtain experimentally. For example, a major surprise of the present work was that the oxygen shift tensors of the bridging carbonyl ligands in $\text{Fe}_2(\text{CO})_9$ have their most deshielded component along the C–O axis. This is highly unusual for a carbonyl ligand, but is the usual behavior observed for organic carbonyl compounds. Moreover, the orientations of the equatorial carbon and oxygen shift tensors in $\text{Fe}(\text{CO})_5$ also differ.

Explanations for these and other observations made in this

(54) Havlin, R. H.; Godbout, N.; Salzmann, R.; Wojdelski, M.; Arnold, W.; Schulz, C. E.; Oldfield, E. *J. Am. Chem. Soc.* **1998**, *120*, 3144–3151. Godbout, N.; Havlin, R.; Salzmann, R.; Debrunner, P. G.; Oldfield, E. *J. Phys. Chem. A* **1998**, *102*, 2342–2350.

work have been given in terms of various analyses of orbital contributions to the shielding tensors. In agreement with previous work, it was found to be necessary to break down the shielding tensors into contributions from different types of localized or delocalized molecular orbitals, or of combinations thereof, depending on the bonding situation. Thus, a “partial IGLO” procedure³⁵ was most successful for the combined localized/delocalized analysis of the shift tensors of bridging ligands in the more complicated cluster compounds. A modified IGLO-PM procedure,³⁶ based on Pipek-Mezey orbital localization,³⁸ also turned out to be particularly useful, due to its inherent σ – π separation. Therefore, while the NMR chemical shift tensor remains a very complicated quantity to study, and simple correlations with other observables are only of limited utility, detailed MO analyses may nevertheless provide important information regarding the dominant electronic and structural origins of the experimental observations.

Finally, we have shown that the agreement between ^{17}O NQCCs of carbonyl ligands obtained from DFT calculations and from solid-state NMR experiments is good. This is another situation where a combination of theory and experiment will be extremely useful for structurally less well characterized materials. We also note that while both chemical shift tensors and ^{17}O NQC tensors in carbonyl ligands are influenced by back-bonding from metal d orbitals into $\pi^*(\text{CO})$ orbitals, their dependence is rather different. This is due to the fact that the NQC tensor is a ground-state property and thus depends only on the character of occupied orbitals and on the nuclear arrangement. In contrast, the chemical shift tensor is a response property, and may be thought of as depending on the characteristics of both ground and excited states of the system.

Acknowledgment. This work was supported by the United States Public Health Service (National Institutes of Health, National Heart, Lung and Blood Institute Grant HL-19481). Work at Stuttgart was supported by Deutsche Forschungsgemeinschaft (“Habilitationstipendium” to M.K.) and by the Max-Planck Gesellschaft. We thank Dr. H. Le for providing his spinning sideband analysis program and Dr. J. Haase for providing his nutation program. We are also grateful to Professor V. G. Malkin and Mrs. O. L. Malkina (Bratislava) and to Professor D. R. Salahub (Montreal) for provision of and assistance with the deMon and deMon-NMR programs.

JA973159T